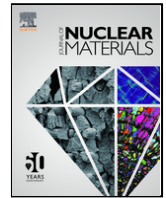




Contents lists available at ScienceDirect

## Journal of Nuclear Materials

journal homepage: [www.elsevier.com/locate/jnucmat](http://www.elsevier.com/locate/jnucmat)

## Role of chemical disorder on radiation-induced defect production and damage evolution in NiFeCoCr

Yufan Zhou<sup>a</sup>, Gihan Veliş̇a<sup>a, b</sup>, Saro San<sup>c</sup>, Miguel L. Crespillo<sup>d</sup>, Zhe Fan<sup>a</sup>, Hongbin Bei<sup>e</sup>, William J. Weber<sup>d</sup>, Pengyuan Xiu<sup>f</sup>, Lumin Wang<sup>f</sup>, F. Tuomisto<sup>g</sup>, Wai-Yim Ching<sup>c, \*</sup>, Yanwen Zhang<sup>a, c, \*\*</sup>

<sup>a</sup> Materials Science and Technology Division, Oak Ridge National Laboratory, Oak Ridge, TN 37831, USA

<sup>b</sup> Horia Hulubei National Institute for Physics and Nuclear Engineering, Măgurele, IF 077125, Romania

<sup>c</sup> Department of Physics and Astronomy, University of Missouri - Kansas City, Kansas City, MO 64110, USA

<sup>d</sup> Department of Materials Science and Engineering, University of Tennessee, Knoxville, TN 37996, USA

<sup>e</sup> School of Materials Science and Engineering, Zhejiang University, Hangzhou 310027, China

<sup>f</sup> Department of Nuclear Engineering and Radiological Sciences, University of Michigan, Ann Arbor, MI 48109, USA

<sup>g</sup> Helsinki Institute of Physics and Department of Physics, University of Helsinki, POB 43, Helsinki 00014, Finland

## ARTICLE INFO

## Article history:

Received 25 November 2021

Received in revised form 23 February 2022

Accepted 27 March 2022

## Keywords:

Radiation

Concentrated solid solution alloys

Defect production

Ion irradiation

## ABSTRACT

Understanding chemical disorder in many concentrated solid solution alloys (CSAs) at the levels of electrons and atoms has attracted increasing attention as a path forward to reveal and identify underlying mechanisms for extraordinary mechanical properties and improved radiation tolerance. Single-phase NiFeCoCr CSA is a common base for many high-entropy alloys (HEAs) that have shown improved mechanical strength and radiation tolerance. In this study, defect production and damage evolution in NiFeCoCr under ion irradiation at room temperature to dose over 20 dpa are determined using ion channeling technique along both  $\langle 100 \rangle$  and  $\langle 110 \rangle$  directions utilizing multiple probing beam energies. The results obtained from the multi-axial and multi-energy channeling analysis are compared with those previously obtained for Ni crystals irradiated under similar conditions. The influence of chemical complexity on defect production and clustering at early-stage under room temperature irradiation up to dose of 1 dpa is discussed based on positron annihilation spectroscopy results. Defect structure evaluation in Ni and NiFeCoCr is also discussed based on transmission electron microscopy results over a prolonged irradiation at both room and elevated temperatures. Compared with chemically complex NiFeCoCr, larger dislocation loops thus less lattice strain are expected to form in pure Ni. Moreover, the role of chemical disorder in this CSA is also investigated based on *ab initio* calculations using large supercells. To understand the impact of chemical complexity effect on defect structure evolution, this integrated research effort attempts to link the relatively large charge redistribution due to difference in valence electron counts resulting from alloying different 3d transition metal elements, moderate lattice distortion arising from similar adaptable atomic size, and notable suppressed or delayed damage evolution in NiFeCoCr.

© 20XX

Edit

Proof

PDF

## 1. Introduction

The development of advanced fission and fusion reactors depends heavily on the robust performance of advanced structural materials under extreme radiation conditions [1–5]. Concentrated solid solution alloys (CSAs), including high entropy alloys (HEAs), which contain two to five principal elements in equiatomic or high concentrations with different elements randomly arranged on a simple crystalline lattice, have demonstrated superior mechanical properties [6–8] and promising radiation resistance [5,9–15]. In the past several years, significant research efforts have been directed towards a fundamental understanding of irradiation-induced damage evolution in single-phase concentrated solid solution alloys (SP-CSAs) [9], for example face-centered-cubic (fcc) based materials including Ni and Ni-based SP-CSAs with increasing complexity [16] at the level of electrons and atoms [9,10], to get a deeper insight into the effects of chemical complexity on energy dissipation and defect evolution under extreme radiation environments.

Among many fcc SP-CSAs, NiFeCoCr is one of the most commonly studied quaternary alloy. NiFeCoCr [17] is usually chosen as a quaternary representative for studying the effects of chemical complexity from the number, size, type and concentration of alloying elements by comparing with pure Ni or other SP-CSAs, which contains 2, 3, or 5 elements (e.g., NiFe, NiCo, NiCoCr, NiFeCoCrAl, NiFeCoCrMn and NiFeCoCrPd) [14,18–26]. Chemical complexity does not monotonically increase with a higher number of alloying elements and the maximum chemical complexity may not occur at the equiatomic composition [9,16]. Chemical complexity, however, does depend on the coupling strengths of alloying elements that involve local electron, magnetic, and phonon interactions [9]. By comparing responses of NiFe, NiCoFe, NiFeCoCr, and NiFeCoCrMn irradiated using 3 MeV Ni at 773 K, Lu et al. [14] have demonstrated that increasing compositional complexity extends the incubation period for void swelling, delays the loop growth and could significantly reduce the segregation phenomenon induced by irradiation. Study in SP-CSAs under Ni irradiation at 300 K<sup>18</sup> reveals that NiCoCr has a comparable irradiation resistance with NiFeCoCr but outperform Ni, NiCo and NiFe. To study the one-dimensional glide of loops mobility, Ni, NiCo, NiFe, NiCoCr, NiFeCoCr, NiFeCoCrMn and NiFeCoCrPd are irradiated with 1 MeV Kr at 773 K [19]. Shi et al. have shown that chemical complexity could influence the mobility of small loops and the mobility is also dependent on the size of the loop itself [19]. By alloying 1 and 3 at% Al in NiFeCoCr, the fabricated alloys Al<sub>0.1</sub>NiFeCoCr and Al<sub>0.3</sub>NiFeCoCr are studied by Yang et al [20,26]. They show that, under high temperature Au irradiation, both alloys exhibit great phase stability and enhanced defect mobility with increasing irradiation temperature [21,26]. To study the He bubble superlattice formation in SP-CSAs, 30 keV He ions were irradiated into Ni, NiFe and NiFeCoCr alloys at room temperature by Harrison et al. [22]. They point out that, in SP-CSAs, the limited 1-D self-interstitial atom diffusion leads to smaller superlattice parameters with smaller bubble diameters.

Notice: This manuscript has been authored by UT-Battelle, LLC, under contract DE-AC0500OR22725 with the US Department of Energy (DOE). The US government retains and the publisher, by accepting the article for publication, acknowledges that the US government retains a nonexclusive, paid-up, irrevocable, worldwide license to publish or reproduce the published form of this manuscript, or allow others to do so, for US government purposes. DOE will provide public access to these results of federally sponsored research in accordance with the DOE Public Access Plan (<http://energy.gov/downloads/doe-public-access-plan>).

\* Corresponding author.

\*\* Corresponding author at: Materials Science and Technology Division, Oak Ridge National Laboratory, Oak Ridge, TN 37831, USA.

E-mail addresses: [chingw@umkc.edu](mailto:chingw@umkc.edu) (W.-Y. Ching), [zhangy1@ornl.gov](mailto:zhangy1@ornl.gov) (Y. Zhang).

Rutherford backscattering spectroscopy in channeling geometry (RBS/C) along only one crystallographic direction (usually along  $\langle 100 \rangle$ ) has been widely applied to SP-CSAs as a main technique for understanding the damage accumulation behavior induced by different ion irradiation at room temperature (300 K) [27–29] and cryogenic temperature (16 K) [30,31]. Unfortunately, multi-axial channeling studies on CSAs have not received so far as much attention as channeling analysis carried out along one crystallographic axis. Recently, by performing multi-axial channeling measurements, Velisa et al. [32] have studied the irradiation-induced damage evolution in Ni as a reference for fcc CSAs. Some ion channeling studies in metals or alloys [32–34] show that if ion channeling analysis is carried out only along one crystallographic direction, the probing beam may not be sensitive to certain types of defects or orientations due to the shadowing effects in crystal lattice. Measurements along multiple channeling directions with variable He<sup>+</sup> beam energies, instead, could provide a more complete scenario on the defects and their migration properties. Therefore, in order to develop a better understanding of the nature of ion irradiation damage in NiFeCoCr fcc SP-CSAs, it is imperative to extend the ion channeling analysis beyond only one major crystallographic axis using monoenergetic He beam. Here, we report a complete study on the irradiation-induced damage evolution in NiFeCoCr based on *in situ* RBS/C along both  $\langle 100 \rangle$  and  $\langle 110 \rangle$  channeling crystallographic orientations.

We investigate defect accumulation and damage evolution in NiFeCoCr, and compare its radiation response with Ni. Although HEAs are considered for advanced nuclear applications, the relevant HEAs being studied remain limited due to the restrictions on the choice of alloying elements in such applications [5]. In this work, NiFeCoCr is chosen as a model system to demonstrate the effect of chemical complexity on defect evolution, rather than as a practical alloy for nuclear application. In addition to the ion channeling analysis, positron annihilation spectroscopy results based on samples irradiated up to 1 dpa at room temperature are compared and discussed, in order to understand the role of chemical disorder on early-stage defect production and clustering. Moreover, we correlate the increase of backscattering and dechanneling yield with radiation-induced strain evolution with modeling insights.

## 2. Experimental details

High quality single crystal NiFeCoCr with  $\langle 100 \rangle$  and  $\langle 110 \rangle$  orientations [35] were used in this study. The crystalline quality of samples was examined using RBS/C before ion irradiations. The NiFeCoCr samples with both orientations were irradiated at room temperature with 1.5 MeV Ni ion under a vacuum of  $5 \times 10^{-5}$  Pa to accumulated fluences of 1, 3, 5, 15, 30, and  $80 \times 10^{14}$  cm<sup>-2</sup> (see Table 1). Adjustable beam slits were used to define an irradiation area. The Ni ion beam was defocused and wobbled in the horizontal and vertical directions with the aim of producing a uniform irradiated region. Beam homogeneity was verified by ion-induced luminescence on quartz targets [36]. To minimize the target heating effects [37] and conduct the irradiation within a reasonable time, the particle flux was set at  $2.1 \times 10^{12}$  cm<sup>-2</sup>s<sup>-1</sup>. During the irradiation, the samples were tilted  $\sim 7^\circ$  off the axial orientations to avoid any undesired channeling effects. Both ion irradiation and *in situ* RBS channeling analysis were performed at the Ion Beam Materials Laboratory (IBML) at the University of Tennessee, Knoxville (USA) [38].

*In situ* RBS/C analysis was utilized to characterize the damage accumulation and evolution after each overlapping Ni irradiation to reach accumulated fluences. For each RBS/C analysis, four different He beam energies from 2.0 to 4.5 MeV (2.0 MeV, 2.7 MeV, 3.5 MeV, and 4.5 MeV) were used to achieve a reasonable energy-dependent analysis for all fluences. In this study, an Iterative Procedure (IP) [39] were used to determine the relative disorder induced by each irradiation.

**Table 1**

The fluences and corresponding doses of 1.5 MeV Ni ion irradiation at 360 nm in Ni and at 424 nm in NiFeCoCr, separately.

Ni		NiFeCoCr	
Fluence (Ni/nm <sup>2</sup> )	Dose (dpa)	Fluence (Ni/nm <sup>2</sup> )	Dose (dpa)
0.7	0.23	1	0.28
1	0.32	3	0.85
3	0.97	5	1.42
20	6.47	15	4.26
100	32.36	30	8.52
		80	22.72

tion condition. This IP has been theoretically validated to analyze not only randomly distributed atoms damage in ceramic, but also the damage in metals and intermetallic alloys [40]. It has been applied to analyze ion irradiated Ni and other fcc CSAs from cryogenic temperature irradiation to high temperature annealing analysis [30–32,41]. The dual-axis and multi-energy RBS/C measurements provide information on damage evolution and defects migration in Ni-irradiated NiFeCoCr with high confidence.

In this work, the irradiation-induced damage profile and injected ion concentration were calculated using SRIM-2013 with full-cascade mode, [42,43] as shown in Fig. 1. SRIM predictions based on Kinchin-Pease mode is also included in Fig. 1 for easy comparison with some literature studies. Threshold displacement energy of 40 eV was chosen for all 4 transition metal elements in NiFeCoCr and 8.144 g/cm<sup>3</sup> was set as sample density [15,35]. Under 1.5 MeV Ni irradiation, the calculated conversion factor at the damage peak (~424 nm) from ion fluence (1 Ni nm<sup>-2</sup> or 1 × 10<sup>14</sup> Ni cm<sup>-2</sup>) to dose in displacements per atom (dpa) is 0.284 (see Table 1). Correspondingly, the conversion factor for additional depths used in this study (see below) are 0.2267 for a depth of 250 nm, and 0.0142 at 788 nm, as marked on Fig. 1.

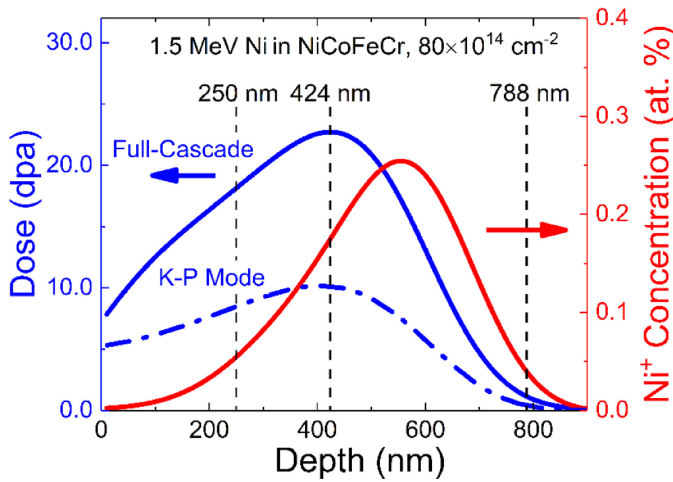


**Fig. 1.** Damage accumulation (left blue axis) and irradiated Ni concentration (right red axis) in NiFeCoCr as a function of depth calculated by SRIM with full-cascade mode (solid line) and Kinchin-Pease mode (K-P mode) (dash dot line). The depth positions at 250 nm, 424 nm, and 788 nm are also marked with dashed line separately (For interpretation of the references to color in this figure legend, the reader is referred to the web version of this article).

**Table 2**

Fully relaxed structure of NiFeCoCr. The average distances of k-nearest neighbors (K-NN) are included. Parameters of fcc Ni are included for comparison.

Ni / CSA	a (Å)	b (Å)	c (Å)	Average (Å)	$\alpha$	$\beta$	$\gamma$	Vol (Å <sup>3</sup> )	1-NN (Å)	2-NN (Å)	3-NN (Å)
Ni	17.563	17.563	17.563	17.563	90.000	90.000	90.000	5417.344	2.484	3.513	4.302
NiFeCoCr	17.512	17.450	17.491	17.484	89.966	90.040	90.028	5344.859	2.473	3.497	4.283

### 3. Modeling details

Pure Ni crystal and NiFeCoCr CSA were constructed using a  $5 \times 5 \times 5$  supercell. The transition metal elements of Cr, Fe, Co, and Ni were randomly distributed in the fcc supercell of 500 atoms to create the solid solution. The relaxation was performed for the CSAs using Vienna Ab initio Simulation Package (VASP) [44]. The electronic convergence criterion is set at  $10^{-5}$  with an energy cutoff of 500 eV, and the force convergence is at  $10^{-3}$  eV/Å for ionic relaxation [45]. The VASP also obtains the elastic tensor calculations based on the stress-strain response scheme [46]. Calculated lattice parameter and bond length from the fully relaxed structure is summarized in Table 2, suggesting no significant lattice distortion.

The Orthogonalized Linear Combination of Atomic Orbital (OLCAO) method [47], also based on the density functional theory (DFT), is efficient for large complex systems due to the ability to evaluate all multi-center interaction integrals. It obtains the electronic structure and bonding analysis, and the use of atomic orbitals enables the evaluation of the bond order (BO) value between a pair of atoms, partial charge (PC) distribution, and the effective charge  $Q^*$  and the associated charge transfer,  $\Delta Q = (Q^0 - Q^*)$ , which is the deviation of the  $Q^*$  from the neutral charge ( $Q^0$ ), based on Mulliken analysis scheme [48].

### 4. Results and discussion

Lattice distortions of Ni and NiFeCoCr have been evaluated both experimentally and computationally in CSAs [49–54]. For a fcc crystal, there are twelve atoms as 1-NNs at a distance of 0.707 of lattice constant ( $a$ ), and six 2-NNs at a distance of the lattice spacing. Lattice distortion in CSAs can be determined from pair distribution function and local lattice strain, defined as  $(a_{1st} - a_{avg})/a_{avg}$ , can be estimated based on the difference between the lattice constant of the local ( $a_{1st}$ ) and average ( $a_{avg}$ ) structures [49,54]. Localized lattice distortion between NiFeCoCr and Ni was previously experimentally determined, as shown in Fig. 2. Insignificant distortion was detected in NiFeCoCr [50], as compared with pure Ni that represents a perfect fcc lattice. The experimentally determined  $a_{1st}$  and  $a_{avg}$  are 3.570 and 3.568 Å for NiFeCoCr, [50,51] while the corresponding values for the reference Ni metal are 3.5237 Å and 3.5242 Å, respectively. The local lattice distortion can be quantitatively compared as a function of the fitting range. The differences  $(a_{1st} - a_{avg})/a_{avg}$  for NiFeCoCr is 0.04%, and the overall little lattice distortion thought is insignificant [50].

The average distances of first nearest neighbors (1-NN), second nearest neighbors (2-NN) and third nearest neighbors (3-NN) suggested from first-principles calculation are listed in Table 2. The lattice distortions, defined as the relative difference ( $\Delta_{k-NN-CSA}$ ) between the CSA and reference Ni,  $(k-NN_{CSA} - k-NN_{Ni})/k-NN_{Ni} \times 100$ , is -0.44, -0.46, and -0.44, respectively. Comparison of the calculated and experimental data of local lattice distortion in the 1-NN, 2-NN, and 3-NN regions is insignificant [45].

The charge transfer ( $\Delta Q$ ) for each atom is an important electronic structural property, which is deviation from the valence electron counts (VECs) of the element. The charge transfer arises from the random site occupation of multiple 3d transition metals with different VEC on the fcc lattice. It can be described by partial charge (PC) distribution and the effective charge  $Q^*$ , which could be obtained from the OLCAO method. While VECs for Cr, Fe, Co and Ni are 6, 7, 9 and 10, their effective charge is different in a CSA environment, shown in Table 3 as 6.28,

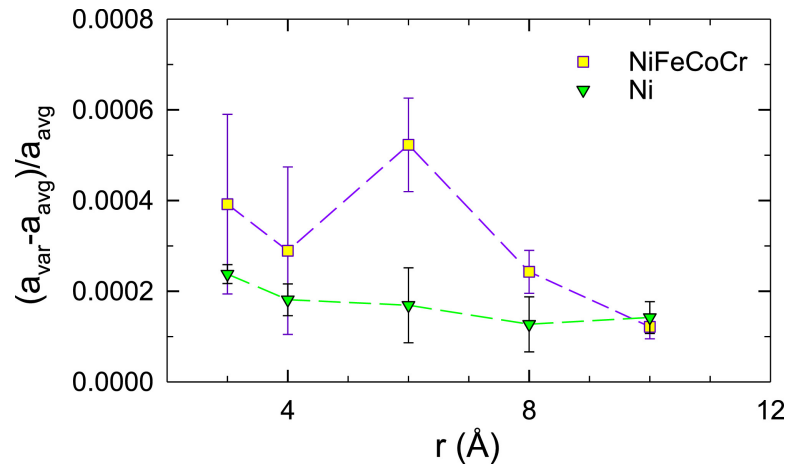


**Fig. 2.** Experimentally determined lattice distortion in fcc NiFeCoCr, CSA, together with pure Ni as a reference. The values and error bars of Ni crystal represent experimental uncertainty of an undistorted fcc structure. Reproduced with permission from Ref. [9]. Copyright 2018 Acta Mater. Inc. Published by Elsevier Ltd.

**Table 3**

Comparison of effective charge ( $Q^*$ ) and partial charge (PC) with the valence electron count for each atom in NiFeCoCr.

TM	Cr		Fe		Co		Ni	
	PC	$Q^*$	PC	$Q^*$	PC	$Q^*$	PC	$Q^*$
NiFeCoCr	-0.28	6.28	0.08	7.92	0.17	8.83	0.03	9.97
VEC	6 ( $3d^5 4s$ [1])		8 ( $3d^6 4s$ [2])		9 ( $3d^7 4s$ [2])		10 ( $3d^8 4s$ [2])	

7.92, 8.83 and 9.97, respectively. Such deviation from the nominal VEC demonstrates that valence electrons will redistribute resulting from interactions with other chemical species in concentrated solution, and such charge redistribution will affect their local structure and atomic volume [9]. It is worth noting that any interpretation in CSAs or HEAs

using VEC for elements in their pure environment may be inadequate or misleading [45].

*In situ* RBS/C spectra of  $\langle 100 \rangle$  and  $\langle 110 \rangle$  NiFeCoCr single crystals irradiated at room temperature with 1.5 MeV Ni to fluence of 1, 3, 5, 15, 30,  $80 \times 10^{14} \text{ cm}^{-2}$  were obtained using 3.5 MeV He beam and shown in Fig. 3a and 3b, respectively. The 3.5 MeV He<sup>+</sup> RBS/C spectra were chosen as mainly study spectra due to the comparability with previous research results on Ni and other Ni based fcc SP-CSAs [15,31,32]. Also, the spectra acquired from random and pristine for both orientations are included to show the fully amorphous and damage-free levels severally. Minimum channeling yield  $\chi_{\min}$  is defined as the ratio of the yield of aligned channel orientation to that of random orientation at the channel number ( $\sim 20$  channels) just behind the surface peak in the spectrum of the pristine crystal. According to the random and pristine spectra in Fig. 3a and b, the  $\chi_{\min}$  for both orientations are less than 5%,

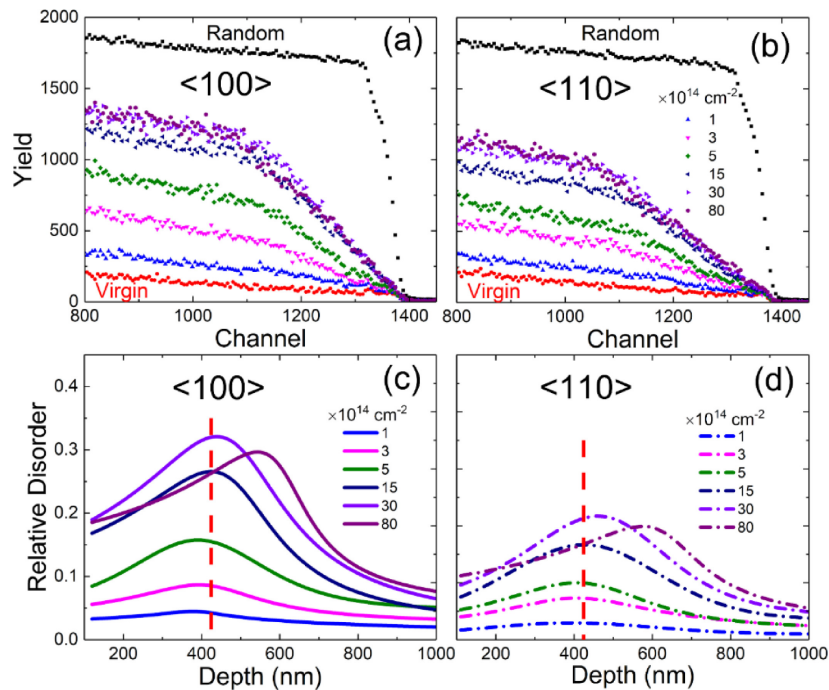


**Fig. 3.** RBS/C spectra probed by 3.5 MeV He<sup>+</sup> along both (a)  $\langle 100 \rangle$  and (b)  $\langle 110 \rangle$  directions of NiFeCoCr CSA after irradiation with different ion fluences from 1 to  $80 \times 10^{14} \text{ cm}^{-2}$ , the random and virgin spectra are also labeled as reference; relative disorder profile vs depth obtained from the RBS/C data by using iterative procedure along (c)  $\langle 100 \rangle$  and (d)  $\langle 110 \rangle$  orientations. The position at 424 nm (damage peak predicted by SRIM full cascade mode) is indicated as the red dashed lines in (c) and (d), and the depth resolution is  $\sim 10$  nm, better in the near surface region and getting worse with the depth due to the increasing energy straggling of the probing beam (For interpretation of the references to color in this figure legend, the reader is referred to the web version of this article).

which indicate that pristine specimens are high-quality single crystals. It is important to note that the Ni-irradiated channeling spectra does not show a clear damage peak and is characterized by an enhanced dechanneling yield that increases with the analyzing depth (i.e., lower channel numbers). This presumably reflects the formation of extended defects (i.e., dislocation loops and stacking fault tetrahedra) [40] in the crystal structure of NiFeCoCr. The formation of extended defects in NiFeCoCr is confirmed based on the energy dependent analysis (see discussion below), which is consistent with previous post-irradiation transmission electron microscopy analysis carried out on fcc CSAs (i.e. 3 MeV Au-irradiated NiFe and NiCo at room temperature) [58].

As mentioned in Section 2, the relative disorder profiles were obtained from the RBS/C spectra using IP [39]. For clarity, only the fitting lines of the data points are shown in Fig. 3c and d for  $\langle 100 \rangle$  and  $\langle 110 \rangle$  NiFeCoCr, respectively. As shown in Fig. 3c, due to the damage accumulation, the relative disorder at 424 nm along  $\langle 100 \rangle$  direction increases initially with the increase of the ion fluence. When the fluence increases to  $30 \times 10^{14} \text{ cm}^{-2}$ , the relative disorder reaches a maximum value and then decreases at depth of 424 nm when the fluence increases up to  $80 \times 10^{14} \text{ cm}^{-2}$ . Therefore, a saturation level around the fluence of  $30 \times 10^{14} \text{ cm}^{-2}$  is evident. In addition, the apparent peak position of the relative disorder shifts to a deeper depth after damage saturation. The apparent disorder peak migrates  $\sim 100 \text{ nm}$  into the sample when Ni fluence increases from  $30 \times 10^{14} \text{ cm}^{-2}$  to  $80 \times 10^{14} \text{ cm}^{-2}$ . Also, it is clearly observed that the relative disorder of  $\langle 100 \rangle$  orientation is always higher than that of  $\langle 110 \rangle$  orientation at the same channel number (i.e. the same depth) with same irradiation condition.

It is worth noting that microstructure analysis based on transmission electron microscopy (TEM) examines inherently a small region, as compared to ion beam analysis with a beam spot over 1 mm in diameter. Aiming at achieving better statistics, ion channeling measurements conducted over sample areas of several millimeters in diameter should have better overall statistics on defect analysis. Works to date have mostly relied on traditional ion channeling analysis carried out along only one crystallographic direction with single He energy [40], to quantify damage accumulation and evolution processes as a function of ion fluence (or dose) in ion-irradiated metals and alloys. Here, RBS/C in conjunction with multiple analyzing beam energies along two major crystallographic orientations is applied to study the irradiation-induced defect evolution in NiFeCoCr. With such approach, we successfully provide unique insight into defect structure evaluation otherwise unavailable using traditional RBS/C (i.e., one He energy). Results from ion channeling measurements and modeling analysis will thus be discussed in more detail below.

#### 4.1. Dose and depth dependence of ion-induced disorder evolution

As discussed above for both orientations (Fig. 3c and d), relative disorders increase initially, then reach saturation at the same fluence value of  $30 \times 10^{14} \text{ cm}^{-2}$  (8.52 dpa). After further Ni irradiation, the relative disorder at 424 nm depth shows a slight decrease with the fluence of  $80 \times 10^{14} \text{ cm}^{-2}$  (22.72 dpa). Both orientations present similar trend with irradiation dose and the relative disorder along  $\langle 100 \rangle$  direction is always higher than  $\langle 110 \rangle$  direction. There are two possible explanations. On one hand, the average atomic spacing along the axial direction will affect the yield of the RBS/C spectrum, [55] which further affects the determination of relative disorder along different axial directions. In NiFeCoCr,  $\langle 100 \rangle$  direction in an fcc structure has relatively narrower channels along the axial (due to higher planar density for the (200) plane) than  $\langle 110 \rangle$  direction with a lower planar density. Relatively narrower channels could cause the increase of the channeling yield along  $\langle 100 \rangle$  axis and further increase the relative disorder analyzed [39]. On the other hand,  $\langle 110 \rangle$  atomic strings may shield some of the defects [32] or less detectable strain due to loop orientation along this orientation [56] which may also cause less dechanneling.

Radiation-induced migration and accumulation of defects to deeper depth, so-called as the “long-range” effect, has been observed in many ion-irradiated materials, including in fcc metals and alloys [58]. The phenomenon has been generally attributed to the high mechanical stress caused by the accumulation of irradiation damage [57–59]. In a recent X-ray diffraction technique (XRD) study, [23] the result shows that Ni irradiation in NiFeCoCr causes small defect clusters at low fluence and produces high lattice strain. Ullah et al. [60] shows that point defects and small clusters in fcc NiFe result in high strain. With further damage accumulation at higher doses and the formation of larger extended defects, the strain is relaxed [60]. The fluence and dose dependence of the relative disorder evolution at a depth of 424 nm (SRIM predicted damage peak position by full cascade mode) along  $\langle 100 \rangle$  and  $\langle 110 \rangle$  axes is plotted in Fig. 4a, and the depth of the apparent disorder peaks identified using the IP approach [39] is shown in Fig. 4b.

The apparent peak disorder positions plotted in Fig. 4b are used to study the damage migration and “long-range” effect in NiFeCoCr, and compared with the phenomenon observed in other fcc CSAs by ion channeling [40] and TEM [58]. It shows in Fig. 4b that for both  $\langle 100 \rangle$  and  $\langle 110 \rangle$  orientation the peak disorder depth keeps steady at around 400 nm at the first three irradiation fluences (1, 3,  $5 \times 10^{14} \text{ cm}^{-2}$ ), then start to shift to a deeper depth under higher fluence ( $15 \times 10^{14} \text{ cm}^{-2}$ ). Further irradiation to 30 and  $80 \times 10^{14} \text{ cm}^{-2}$  leads to further shift of the apparent damage peak.

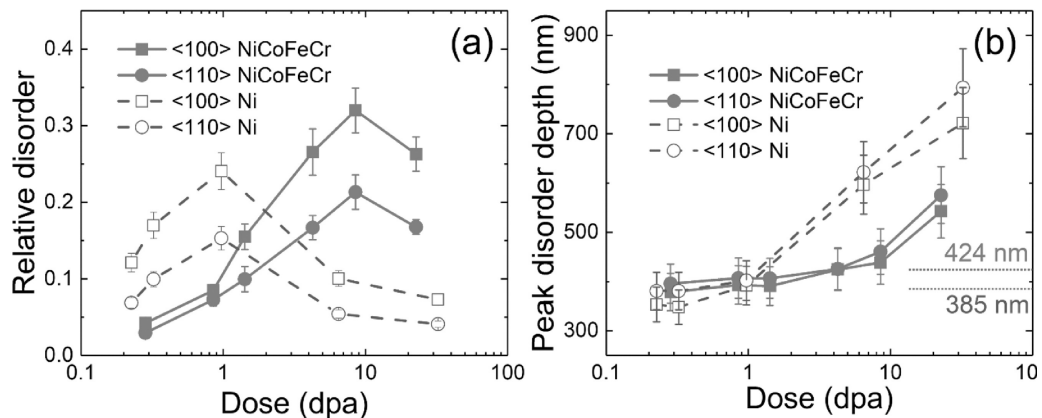


**Fig. 4.** (a) Damage accumulation for 1.5 MeV Ni irradiated NiFeCoCr (at the depth of 424 nm) and Ni (at the depth of 385 nm) and (b) depth of apparent peak disorder in NiFeCoCr and Ni as a function of dose for both  $\langle 100 \rangle$  and  $\langle 110 \rangle$  orientations based on 3.5 MeV He<sup>+</sup> RBS/C spectrum. For Ni and NiFeCoCr crystals before irradiation, the relative disorder is zero, the reference point. SRIM predicted damage peak position are also marked out in (b).

#### 4.2. Defect evolution (I): energy dependent at the damage peak (424 nm)

It is known that each type of ion irradiation produced defects has a particular influence on the analyzing He<sup>+</sup> beam with different energy (i.e., direct backscattering or enhanced dechanneling of the probing beam), information of defects in materials can be extracted by analyzing the RBS/C spectra collected by varying He<sup>+</sup> probe energies [32,55,61,62]. More specifically, the correlation between the disorder and square root of the probing beam energy ( $E^{1/2}$ ) is the key indicator: [32] (i) A linear relationship with positive slope means that the defect type consists mainly of extended defects (dislocation loops or dislocation lines, mainly attributed to the size of dislocations or the number of interstitials involved); (ii) the linear relationship with a negative slope indicate that the observed damage structure comprises uncorrelated displaced lattice atoms (for example, interstitials, vacancies or amorphous clusters); (iii) for discontinuous defects (such as stacking faults or voids) in damaged materials, the disorder and square root of the energy ( $E^{1/2}$ ) of the probe beam are uncorrelated with each other (slope equals to 0). Therefore, to investigate the evolution of the defects under different damage condition in NiFeCoCr, the energy dependent ion channeling studies were conducted along both  $\langle 100 \rangle$  and  $\langle 110 \rangle$  orientations at 4 probing beam energies and 6 different irradiation fluences from 1 to  $80 \times 10^{14} \text{ cm}^{-2}$ .

The disorder variation versus the  $E^{1/2}$  of the probe He<sup>+</sup> at the SRIM predicted damage peak depth (424 nm) along both  $\langle 100 \rangle$  and  $\langle 110 \rangle$  orientations are shown in Fig. 5. In Fig. 5a and b, the fitting lines of the relative disorder values associated with each irradiation condition show that the overall disorder and  $E^{1/2}$  dependence present a positive correlation with different slope value under all analyzed irradiation conditions. For both orientations, there are two different sets of slope values: for lower irradiation fluences (1, 3,  $5 \times 10^{14} \text{ cm}^{-2}$ ) the slopes' values are much smaller compared with the higher fluences (15, 30,  $80 \times 10^{14} \text{ cm}^{-2}$ ) irradiation conditions.

To get a clearer trend of the slope variation, the slope values as a function of fluence were plotted in Fig. 5c. It shows that, with the relatively low irradiation fluence 1, 3 and  $5 \times 10^{14} \text{ cm}^{-2}$ , the slope values for both orientations are rather constant with a relative low level (lower than 0.05). However, when the fluence accumulated from  $5 \times 10^{14} \text{ cm}^{-2}$  to  $15 \times 10^{14} \text{ cm}^{-2}$ , the slopes come up to around 0.1 for both directions and then keep increasing with the increase of the irradiation fluence. Based on the energy dependent theory [55,62], the results show that, at the beginning of the damage accumulation (lower irradiation fluence region), the defects at 424 nm consists of mainly small defect clusters (combination of several types of defects, such as point defects, defect clusters or small dislocations). Under these low fluence irradiation conditions, the small extended defects may be one of the most important configurations but not significant since the slope values are positive but relatively small. When the fluence reaches to

$15 \times 10^{14} \text{ cm}^{-2}$ , the slopes increase dramatically along both directions, which indicates that the extended defects become dominant and lead to increased dechanneled probing He<sup>+</sup> beam. There are two reasons which may cause such slope change: on the one hand, additional Ni irradiation cause more local damage and more small clusters are created, which also include more extended defects formation in damaged region; on the other hand, more localized damage accumulation will introduce more lattice strain/distortion which triggers the growth of extended defects (dislocation lines or large loops, or both) [32,63]. For both orientations, the slope values increase at the fluence of  $15 \times 10^{14} \text{ cm}^{-2}$ , which means there is no significant difference in irradiation damage induced extended defect formation, configurations or shadowing effects on  $\langle 100 \rangle$  and  $\langle 110 \rangle$  direction. Dislocation loop configurations (i.e., perfect and faulted loops) and orientations in irradiated fcc CSAs are characterized and discussed [56].

On-zone scanning transmission electron microscopy (STEM) via both bright-field (BF) and annular dark field (ADF), for effective and convenient dislocation loop imaging characterization based on projected morphology, [56,64] is extended from irradiated bcc ferritic based alloys [65] to irradiated fcc materials [56,66]. This on-zone STEM methodology [56] applied to irradiated fcc materials has been validated by comparing with several traditional techniques, including two-beam condition imaging in both conventional TEM (CTEM) [56] and STEM [66] modes, as well as rel-rod dark-field imaging in CTEM mode. [56] All perfect and faulted loops of types  $a/2 \langle 110 \rangle \{110\}$  and  $a/3 \langle 111 \rangle \{111\}$  in an ion irradiated Ni<sub>40</sub>Fe<sub>40</sub>Cr<sub>20</sub> CSA were simultaneously imaged, and their types, configurations and populations were characterized with high accuracy, [56] TEM characterization on some Ni-based SP-CSAs [66] also reveals that, with increasing irradiation fluence, some faulted loops are expected to transform into perfect loops, and the fraction of faulted loops decreases as perfect loops increase. The study of dislocation loops along [001], [011] and [111] zones [56] also confirms the effectiveness of the ion channeling investigation along  $\langle 100 \rangle$  and  $\langle 110 \rangle$  orientations in this work.

Based on the energy dependent analysis (Fig. 5c) and discussions above, the relative disorder (Fig. 4a) and the apparent peak damage position (Fig. 4b), one can reach some conclusions regarding damage accumulation and defects evolution in NiFeCoCr under 1.5 MeV Ni irradiation. Based on the data at depth of 424 nm, at the beginning of the irradiation with low irradiation fluence of 1, 3,  $5 \times 10^{14} \text{ cm}^{-2}$ , the energetic Ni ions only cause scattered defects, including small extended defect clusters resulting directly from displacement cascades [9]. This proposition is confirmed by atomistic simulations and earlier irradiation experiments [23,67]. Small extended defect clusters may contain interstitial atoms ranging from a few to a few tens of atoms that are revealed by molecular dynamics (MD) simulations [23,67] and up to a few nm in size observed under TEM [67]. The work further shows that, in irradiated fcc Ni, NiFe, and Ni<sub>0.8</sub>Cr<sub>0.2</sub>, irradiation-induced intersti-

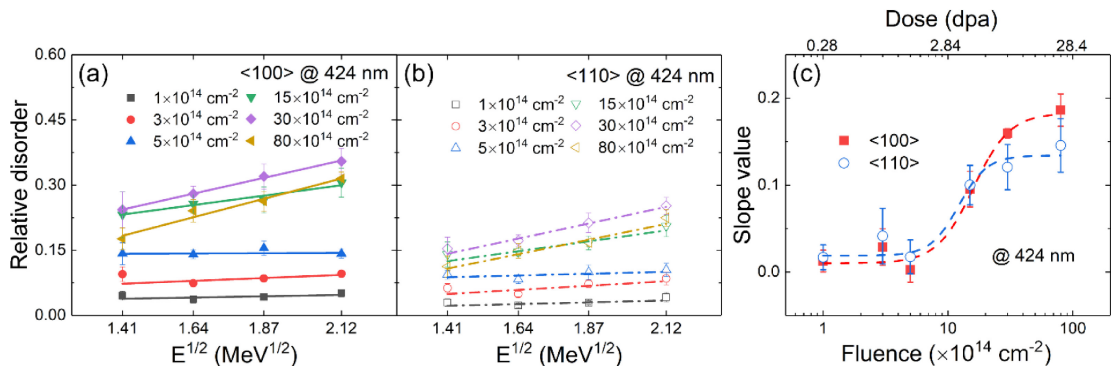


**Fig. 5.** Relative disorder along (a)  $\langle 100 \rangle$  and (b)  $\langle 110 \rangle$  versus the square root energy of the analyzing He ion at the depth of 424 nm in irradiated NiFeCoCr with fluence from 1 to  $80 \times 10^{14} \text{ cm}^{-2}$ . The solid and dash dot lines are linear fits. (c) The slope value of the energy dependence at 424 nm versus the Ni irradiated fluences from 1 to  $80 \times 10^{14} \text{ cm}^{-2}$  for both  $\langle 100 \rangle$  and  $\langle 110 \rangle$  directions. The dashed lines are fitted with logistic function to guide the eyes.

tials form dislocation loops that are of  $a/3\langle 111 \rangle\{111\}$ -type. While the loops are formed in all the three crystals, the kinetics of formation revealed by molecular dynamics simulation is considerably slower in NiFe and Ni<sub>0.8</sub>Cr<sub>0.2</sub> than that in pure Ni, leading to smaller cluster sizes in the alloys compared to pure Ni. As for the current study in irradiated NiFeCoCr with pure Ni as a reference, similar arguments should hold. Under this condition, the scattered defects are far from each other so that little interaction between them, and the lattice distortions/strains accumulate but not high enough to trigger the growth of small defect clusters. This interpretation is supported by an earlier study in irradiated Ni, NiFe and NiFeCoCr under Ni irradiation at room temperature [23]. The integrated XRD technique and MD simulations show that the elastic strain can be quantified in irradiated Ni and the SP-CSAs. As the change in the lattice parameter is related to the relaxation volume of the defects at the origin of the elastic strain, the strain can be treated as a sensor to monitor the defect evolution under irradiation [23]. Damage evolution is investigated as a function of increasing ion fluence via elastic strain developed in the irradiated crystals, and the results indicate that the size and density of interstitial-type defect clusters, primarily detected by changes in elastic strain level, increase with the ion fluence. The increasing net positive elastic strain identified in NiFe and in NiFeCoCr with ion fluence up to  $1 \times 10^{14} \text{ cm}^{-2}$  implies that contributions from both vacancy and interstitial type defects do not cancel out, and strain from interstitial dislocation loops is more noticeable. Smaller defect clusters are formed in the two CSAs and result in an increase in the net elastic strain, which increases with ion fluence due to the increasing density of defect clusters. They further point out that the strain level is expected to reduce/relax at high ion fluence as the defect concentration saturates and defects or clusters start to interact and evolve. These previous results support what is detected from *in situ* RBS measurements in the current study. With further irradiation to  $\sim 15 \times 10^{14} \text{ cm}^{-2}$ , accumulated defects clusters increase in density and start to overlap. Moreover, the radiation-induced lattice strain reaches to a threshold that lattice distortions/strains are high enough to trigger the evolution of the small defect clusters. Radiation-induced lattice strains may be interpreted differently as the strain measurements and determination depend on defect type, size and number, as well as the length scale (e.g., at a single defect or statistically over a large sample volume). Earlier work reveals that in ion-irradiated metals, dislocation loops produced from ion irradiation may have different strain field, and high local density of the nano-scale loops will drive spatial ordering of these loops [68]. The existence of dense loops implies that the average distance between defect clusters is small, and the loop ordering may spontaneously result from the combined action of angular-dependent elastic interaction between the loops and stochastic Brownian motion (diffusion) of loops. Similar to elastic strain detected by XRD, ion channeling technique is sensitive to lattice imperfection or small defect clus-

ters (e.g., direct backscattering by interstitials or greater dechanneling ions due to changes of atomic potential resulting from the existence of vacancies) over a relatively larger volume. Rather than strain field associated with individual defect types or dislocation loops [68], damage evolution detected via *in situ* RBS over a larger volume, such as at the length scale of tens of nm, provides information on a statistical response of defect evolution. Nevertheless, based on a recent study using binary collision approximation simulating RBS/C spectra from MD atom coordinates of irradiated cells, [69] the defect evolution monitored by RBS/C is mainly attributed to the size of dislocations and the number of interstitials involved. Though the formed extended defects could release some certain lattice distortions/strains, the overall lattice distortion/strains are still increasing which cause the relative disorder increasing till  $30 \times 10^{14} \text{ cm}^{-2}$  for both  $\langle 100 \rangle$  and  $\langle 110 \rangle$  orientations. With the continuous increase of the damage induced by Ni irradiation, the lattice distortions/strains increase, and larger extended defects are formed. When a disorder saturation stage is achieved (more than  $30 \times 10^{14} \text{ cm}^{-2}$ ), complex dislocation networks are formed [13,63] and a release of accumulated lattice distortions/strains takes place. As a result, the energy dependent slope keeps increasing and the relative disorder decreases, as the observation under  $80 \times 10^{14} \text{ cm}^{-2}$  irradiation (Figs. 4a and 5c).

#### 4.3. Defect evolution (II): energy dependent at 250 nm and 788 nm

The “long-range” effect suggests that dislocation loops would migrate both towards the surface and deeper into samples if mechanical stress is large enough for enhancing dislocation motion [27]. To study the defect evolution and identify possible anisotropic damage behavior at both shallower and deeper depths, a depth closer to the surface at 250 nm was chosen to represent the position between the surface (with an  $\sim 80\%$  dpa compared with the most damaged position at 424 nm). A deeper depth at 788 nm ( $\sim 5\%$  dose ratio comparing with the dose at 424 nm) was chosen as a representative of defect activities near the end of ion range (see Fig. 1). The energy dependent analysis was applied for both two depths with two orientations, the slope of disorder variation versus the  $E^{1/2}$  of the probe He<sup>+</sup> as a function of Ni fluence were plotted in Fig. 6a and b for the depth of 250 nm and 788 nm, respectively.

As shown in Fig. 6a, the slope change at 250 nm has a similar trend with the one at 424 nm. At first 3 lower fluences (1, 3, and  $5 \times 10^{14} \text{ cm}^{-2}$ ), the slopes keep nearly constant at a relatively small positive value, indicating the presence of mainly small defect clusters. When the fluence reaches to  $15 \times 10^{14} \text{ cm}^{-2}$ , the slopes show a clear increase on both directions, suggesting that the extended defects become more dominant with such irradiation conditions at this depth.

Inspection of the results at the depth at 788 nm, Fig. 6b, the slope changes between  $\langle 100 \rangle$  and  $\langle 110 \rangle$  direction is different from the

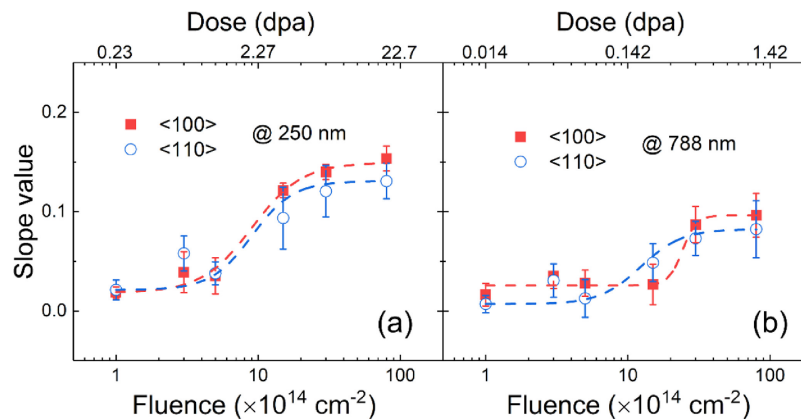


Fig. 6. The slope value of the energy dependence at the depth of (a) 250 nm and (b) 788 nm versus the Ni irradiated fluences from 1 to  $80 \times 10^{14} \text{ cm}^{-2}$  for both  $\langle 100 \rangle$  and  $\langle 110 \rangle$  directions in NiFeCoCr CSA. The dashed lines are fitted with logistic function to guide the eyes.

dependence at 250 nm and 424 nm. For  $\langle 110 \rangle$  orientation, similar as the trend at both 424 and 250 nm depth, the slope value shows increase with a fluence of  $15 \times 10^{14} \text{ cm}^{-2}$ . However, for  $\langle 100 \rangle$  orientation, such increase does not start or become obvious until  $30 \times 10^{14} \text{ cm}^{-2}$ , indicating that, at 788 nm with a fluence of  $15 \times 10^{14} \text{ cm}^{-2}$  along  $\langle 100 \rangle$  direction, the extended defects may dechannel less probing He ions than those along  $\langle 110 \rangle$  direction. What should be noticed is that the damage dose is 1.14 dpa at 788 nm for fluence of  $80 \times 10^{14} \text{ cm}^{-2}$ , which is lower than the dose at 424 nm with a fluence of  $5 \times 10^{14} \text{ cm}^{-2}$  (1.42 dpa). According to the discussion in Section 4.2, at 424 nm with the fluence of  $5 \times 10^{14} \text{ cm}^{-2}$ , large extended defects are not the dominant defect-type. The extended defects detected at 788 nm with higher irradiation fluences are, thus, high likely formed due to the “long-range” effect. For an fcc system, the Burgers vector of the lowest energy dislocation is  $\frac{1}{2}\langle 110 \rangle$ , which is easier to be formed due to large lattice distortions/strains. The delay of the slope increasing along  $\langle 100 \rangle$  compared with the one along  $\langle 110 \rangle$  can be explained that He<sup>+</sup> passing along  $\langle 110 \rangle$  axis will directly interact with the dislocation formed by the early stage of “long-range” effect. It indicates that at 788 nm the extended defects caused by “long-range” effect may have preference along different crystallographic orientations and be viewed differently by TEM and discussed elsewhere [56].

#### 4.4. Comparison of radiation-response in Ni and NiFeCoCr

Velisa et al. studied the irradiation-induced damage evolution in single crystal fcc Ni [32]. For comparison, relative disorder at the peak depth (385 nm predicted by SRIM full cascade mode) and the depth of the apparent peak disorder are also plotted in Fig. 4a and b, respectively. The irradiation fluences and doses with 1.5 MeV Ni ions in pure Ni and NiFeCoCr are listed in Table 1 for reader's convenience. From Fig. 4a, under 1.5 MeV Ni irradiation, the damage accumulated in Ni along both  $\langle 100 \rangle$  and  $\langle 110 \rangle$  orientation shows similar trend with NiFeCoCr but clearly evolves more rapidly with increasing dose than that in NiFeCoCr. The damage in pure Ni reaches saturation at 0.97 dpa (at fluence of  $3 \times 10^{14} \text{ Ni cm}^{-2}$ ) with a relative disorder of 0.24 for  $\langle 100 \rangle$  orientation and 0.15 for  $\langle 110 \rangle$  orientation. For NiFeCoCr CSA, the damage saturation dose is 8.52 dpa ( $30 \times 10^{14} \text{ cm}^{-2}$ ) with relative disorder at 0.32 for  $\langle 100 \rangle$  orientation and 0.21 for  $\langle 110 \rangle$  orientation. The comparison suggests that chemically complex NiFeCoCr has intrinsically higher mechanical strength that tolerant the higher lattice distortions/strains and can more effectively suppress damage accumulation. The modeling work in Tables 2 and 3 shows that intrinsic lattice distortion is insignificant in NiFeCoCr, which is sup-

ported with x-ray diffraction results shown in Fig. 2, but difference in VECs is noteworthy as these transition metals are neighbors in period 4 in the periodic table. The improved mechanical strength and delay of damage accumulation should be mainly attributed to the relatively large difference in VECs. The noticeable partial charge distribution (Table 3) among the neighboring atoms in fcc lattice leads to a perceptible electronic deformation ability, which can significantly modify defect energetics, as discussed in a recent review [9], and result in better radiation resistance.

In Fig. 4b, the apparent damage peak position in pure Ni is shallower than that in NiFeCoCr at very early damage status. With the increasing of the damage dose, the damage peak shift appears at lower damage dose (0.97 dpa,  $3 \times 10^{14} \text{ cm}^{-2}$ ) for pure Ni than the dose (4.26 dpa,  $15 \times 10^{14} \text{ cm}^{-2}$ ) for NiFeCoCr. The damage peak locates much deeper in pure Ni than in NiFeCoCr under higher damage dose conditions. It reveals that the “long-range” effect starts with lower dose in Ni than in NiFeCoCr and affects larger area under the same damage dose, which further proves that the NiFeCoCr alloy has higher mechanical strength than pure Ni and could suppress the “long-range” effect under same damage condition. In other words, small defect clusters are more mobile [9] in Ni than in NiFeCoCr and thus, the formation of larger defects is expected in Ni.[9,74]

Vacancy-type defects in Ni and NiFeCoCr under irradiation are studied using positron annihilation spectroscopy (PAS) [70]. The positron annihilation parameters  $S$  and  $W$  are shown in Fig. 7 as a function of the irradiation dose ranging from 0.01 to 1 dpa. While sensitive to vacancy-type defects, positrons are also sensitive to the chemical identities of atoms surrounding the vacancies [9,70,71]. The pristine Ni and NiFeCoCr crystals before irradiation are marked in the figure as the reference points that have the lowest  $S$  and the highest  $W$  values, reflecting the longest effective positron diffusion length and the shortest positron lifetime, respectively. Compared with these reference points in Fig. 7, PAS signals from the irradiated samples appear into two groups, near the middle of the plot for Ni and towards the bottom right part of the plot for the CSA. Increasingly, a different dose dependence is observed from irradiated Ni and NiFeCoCr. The CSA clearly shows a dose dependence that the value of the  $S$  parameter decreases but the value of  $W$  increase with increasing dose. In other words, the  $S$ - $W$  data sets move towards upper left corner of the plot. Little dose dependence is observed for irradiated Ni, suggesting that the vacancy-type defect production and evolution are saturated in Ni already at the lowest doses. In chemically complex NiFeCoCr, the clear dose dependence is due to the radiation-induced change of the local chemical environment, suggesting that segregation may occur at the atomic scale already in the very early stages of radiation damage accumulation [70].

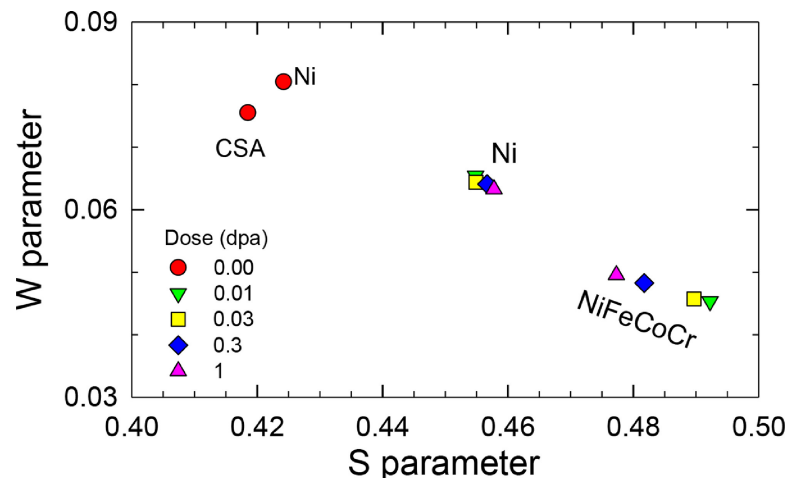


Fig. 7. Comparison of ( $S$ ,  $W$ ) parameters for pure Ni and NiFeCoCr CSA, both the pristine samples (upper left corner) and the irradiated samples with increasing radiation dose.

Through energy dependent analysis, the study on Ni also reveals that, at high fluence irradiation stage ( $100 \times 10^{14} \text{ cm}^{-2}$  in their case), the dependence of the relative disorder as a function of  $E^{1/2}$  along both  $\langle 100 \rangle$  and  $\langle 110 \rangle$  directions have a linear relation with positive slope, indicating that extended defects are dominant under such conditions. However, at lower fluence irradiation ( $1 \times 10^{14} \text{ cm}^{-2}$ ), the type of defects is different. On one hand, along  $\langle 110 \rangle$  direction the disorder on  $E^{1/2}$  has a linear relation with positive slope at the damage peak position with the dose of  $1 \times 10^{14} \text{ cm}^{-2}$ , which is similar as the results in NiFeCoCr. On the other hand, a linear relation with negative slope was observed along  $\langle 100 \rangle$  orientation, suggesting that more displaced atoms (interstitials or vacancies) are encountered along this direction. Such different types of defects are also reported by Sellami et al. from XRD analysis in Ni and NiFeCoCr alloy under low fluence Ni irradiation ( $1 \times 10^{14} \text{ cm}^{-2}$ ) [23], where this technique presents a relevant sensitivity to detect small defect clusters produced at low fluences. According to their analysis, a wide defect spectrum may exist in irradiated Ni which leads to a net zero strain, however, a net positive elastic strain observed for NiFeCoCr implies that the interstitial dislocation loops seem to dominate [23]. One possible explanation for this evidence is that, compared with Ni, chemical complexity in NiFeCoCr CSA could modify point defect energetics [9,72,73] and sluggish defect and cluster migration [9,74,75]. As a result, more defects, especially the small interstitials or interstitials cluster, will be trapped locally and form small extended defect clusters in NiFeCoCr. In a Ni crystal with little or none chemical disorder on an ideal fcc lattice, small defect clusters are more mobile [9,13] and the interstitial-vacancy recombination rate is lower than NiFeCoCr which leads to different defects spectrum. Zhao et al. reported positive and negative stacking fault energy (SFE) for Ni and NiFeCoCr, respectively [76]. It is expected that positive SFE values to assist/favor clustering, while negative SFE values presumably show a tendency towards ordering.

Influence of injected interstitials has been reported in conventional alloys [77–80] and SP-CSAs [81]. Energetic ions lose energy to electrons in the matrix, initiating athermal/inelastic processes, and to nuclei, resulting in displacement damages via collision cascades; [11] and come to rest at the end of the ion range as interstitial atoms. Injected interstitials may result in suppression of void swelling and drastically modify the precipitation behavior, [80] all depend sensitively to elevated temperature and dose rate. Influence of injected Ni interstitials on void swelling were investigated in Ni and three SP-CSAs (NiCo, NiFe and NiFeCoCr) under 3 MeV Ni irradiation at 500 °C [81]. Cross sectional TEM characterization of the void formation and void denuded zones suggests that the suppression effect from injected interstitials is most pronounced in Ni and NiCo. The relatively less influence observed in NiFe and NiFeCoCr is attributed to the 3-dimensional sluggish interstitial movement, which is different in nearly 1-dimensional movement in Ni and NiCo [9,13,81]. In an irradiated material, the injected ion concentration varies with depth. Under the current irradiation condition, the injected Ni will peak at  $\sim 550 \text{ nm}$ , as shown in Fig. 1. For the highest fluence, the injected Ni concentration is approaching 0.3 at% at the peak. While the concentration of injected interstitials is noticeable, the effect is expected to be negligible as irradiations were conducted at room temperature.

#### 4.5. Comparison with other materials that are difficult to be amorphized

Single crystals as Ni and NiFeCoCr are difficult to be amorphized, similarities in radiation responses are also observed in some radiation-resistant oxides. Damage evolution in YSZ [82] and MgO [83] is studied by combining XRD and RBS/C analysis. According to the analysis, both YSZ and MgO follow a three step Multi-Step Damage Accumulation (MSDA) model described by Jagielski and Thomé [84] Point defects and small defect clusters, which induce a low disorder level in RBS/C but a significant strain level, are likely formed during the first step. The

sharp increase in the damage yield occurring during Step 2 corresponds to the formation of dislocation loops, which progressively merge into a dense network of dislocations that further induces a plastic relaxation of the elastic strain. The surprising decrease of the disorder level during Step 3 may be attributed to the reorganization of the tangled and disordered dislocations into a network of long dislocations acting as defect sinks where small defects are trapped and therefore inducing the formation of slightly damaged regions [85]. Similar trend of damage evolution has also been recently observed in  $\text{UO}_2$  [86]. Both experimental and modeling work have demonstrated that the final status of the radiation-resistant oxides (e.g., YSZ (Fm3m) [63,83] and MgO (Fm3m) [83]) and many metal alloys (e.g., Cu, Ni, and Ni-based SP-CSAs [24,27,29,31,32]) is associated with dislocation network formation. On the other hand, the radiation-sensitive ceramics (e.g., SiC [87] and  $\text{LiNbO}_3$  [88,89]) usually form point defects or amorphous defect clusters instead of dislocations. Damage overlapping in such radiation-sensitive materials could not transform defect clusters into extended dislocation loops or dislocation lines. As a result, the disorder or small defects will grow in the damage area upon further irradiation and eventually form an amorphous layer.

Similar to the case of radiation-resistant oxides, MSDA analysis was performed to reveal damage kinetics for ion-irradiated Ni-based SP-CSAs (i.e., Ni, NiFe and NiFeCoCr) at 16 and 300 K [15,28,30]. In the case of elemental Ni, single step accumulation kinetics is observed and may be interpreted by a simple Gibbons model. In the case of NiFe and NiFeCoCr alloys irradiated at 300 K, the analysis of the damage build-up is well interpreted with a two-step damage accumulation kinetics assuming that the sharp increase in the damage yield occurring during Step 2 corresponds to the transition of dumbbells to dislocation loops or small loops, and then to large loops. In this study, in the second step, the disorder increases with irradiation fluence until the disorder reaches a maximum value; after this maximum, the disorder starts to decrease (determined from the ion channeling perspective) which can be related to the presence of complex dislocation networks. Previous experimental and modeling works in NiFeCoCr [13,17,19,24] have demonstrated that, under high fluence irradiation, small defect clusters or dislocation loops evolve to complex dislocation networks. This, in turn, will release the accumulated irradiation-induced strain and reduce the overall relative disorder measured by RBS/C. Finally, it is important to emphasize that the analysis of the energy-dependent RBS/C characterization along different crystallographic orientations carried out in this work provide strong support to previous interpretations of disordering kinetics in ion-irradiated NiFeCoCr, that were based on merely phenomenological descriptions of RBS/C data (e.g., MSDA model).

Advancing material sciences demands integration of experimental measurements with computational modeling whenever possible. With the increased interplay between experimental and computational approaches at multiple length scales, better understanding may be achievable. The integrated modeling effort based on *ab initio* calculations and the experimental approaches, including ion irradiation, ion beam analysis, microscopy and spectroscopy techniques, establishes a powerful path forward to understanding the role of chemical disorder on radiation-induced defect production and damage evolution, and to obtain a more complete quantitative description.

## 5. Conclusion

Building upon on relevant TEM and XRD results in literature, we investigate the role of chemical disorder on radiation-induced defect production and damage evolution by comparing Ni with NiFeCoCr using *in situ* RBS channeling technique, positron annihilation spectroscopy and large supercell *ab initio* calculations. Defect accumulation and structural evolution induced by 1.5 MeV Ni irradiation in NiFeCoCr along both  $\langle 100 \rangle$  and  $\langle 110 \rangle$  crystallographic orientations have been

studied using *in situ* ion channeling method. Three regions have been clearly identified. At the beginning of the irradiation (up to  $5 \times 10^{14} \text{ cm}^{-2}$  1.42 dpa), only several localized small defect clusters are generated. When the irradiation damage reaches a certain critical level ( $15 \times 10^{14} \text{ cm}^{-2}$  or  $\sim 4.26$  dpa), the irradiation-induced damage and lattice strains are high enough to trigger the evolution of small defect clusters to form extended defects. With the increase of damage induced by further Ni irradiation (higher than  $30 \times 10^{14} \text{ cm}^{-2}$  or  $\sim 8.52$  dpa), entangled dislocation networks are formed that releases the accumulated lattice strains. As a result, the energy dependent slope keeps increasing and the relative disorder decreases. According to the energy dependent analysis at 788 nm along different orientations, the migrated extended defects caused by “long-range” effect may have preference at the early stage, which has not been hitherto reported in ion channeling studies performed on irradiated NiFeCoCr. In comparison with Ni, the integrated experimental and modeling effort calls attention to chemical disorder by associating the relatively large charge redistribution and insignificant lattice distortion with the notable suppressed or delayed damage evolution in NiFeCoCr.

This study focused on a typical fcc structure quaternary SP-CSA, NiFeCoCr, reveals the role of chemical disorder on damage accumulation and defects evolution, and provide important information for supporting Ni-based SP-CSAs and HEAs as strong candidates in future technological applications designed to keep stable structural properties and enhanced tolerance in harsh environments.

#### Data availability

The raw and processed data required to reproduce these findings will be made available upon request.

#### Uncited references

[25].

#### CRedit authorship contribution statement

**Yufan Zhou:** Investigation, Methodology, Formal analysis, Writing – original draft, Writing – review & editing. **Gihan Veliša:** Methodology, Formal analysis, Writing – original draft, Writing – review & editing. **Saro San:** Investigation, Methodology. **Miguel L. Crespillo:** Investigation, Writing – review & editing. **Zhe Fan:** Investigation, Writing – review & editing. **Hongbin Bei:** Resources, Writing – review & editing. **William J. Weber:** Visualization, Writing – review & editing. **Pengyuan Xiu:** Investigation, Writing – review & editing. **Lumin Wang:** Writing – review & editing. **F. Tuomisto:** Investigation, Methodology, Writing – review & editing. **Wai-Yim Ching:** Methodology, Writing – review & editing, Project administration. **Yanwen Zhang:** Conceptualization, Visualization, Methodology, Validation, Writing – original draft, Writing – review & editing, Supervision, Project administration.

#### Declaration of Competing Interest

The authors declare that they have no known competing financial interests or personal relationships that could have appeared to influence the work reported in this paper.

#### Acknowledgment

This work was supported as part of the Energy Dissipation to Defect Evolution (EDDE), an Energy Frontier Research Center funded by the US Department of Energy, Office of Science, Basic Energy Sciences under contract number DE-AC05-00OR22725. The ion irradiations were

performed at the Ion Beam Materials Laboratory located at the University of Tennessee, Knoxville.

#### References

- [1] T. Allen, J. Busby, M. Meyer, D. Petti, Materials challenges for nuclear systems, *Mater. Today* 13 (12) (2010) 14–23.
- [2] S.M.R. Gilbert, K. Arakawa, Z. Bergstrom, M.J. Caturla, et al., Perspectives on multiscale modelling and experiments to accelerate materials development for fusion, *J. Nucl. Mater.* 554 (2021) 153113.
- [3] Elizabeth Gibney Fuel for world's largest fusion reactor ITER is set for test run, Nuclear fusion experiments with deuterium and tritium at the joint European Torus are a crucial dress rehearsal for the mega-experiment, *Nature* 591 (2021) 15–16, <https://doi.org/10.1038/d41586-021-00408-1>.
- [4] M. Granger Morgan, A. Abdulla, M.J. Ford, M. Ratha, US nuclear power: the vanishing low-carbon wedge, *Proc. Natl Acad. Sci.* 115 (28) (2018) 7184–7189, <https://doi.org/10.1073/pnas.1804655115>, first published July 2, 2018.
- [5] E.J. Pickering, A.W. Carruthers, P.J. Barron, S.C. Middleburgh, D.E.J. Armstrong, A.S. Gandy, High-entropy alloys for advanced nuclear applications, *Entropy* 23 (2021) 98, <https://doi.org/10.3390/e23010098>.
- [6] B. Gludovatz, A. Hohenwarter, D. Catoor, E.H. Chang, E.P. George, R.O. Ritchie, A fracture-resistant high-entropy alloy for cryogenic applications, *Science* 345 (6201) (2014) 1153–1158.
- [7] Z. Li, K.G. Pradeep, Y. Deng, D. Raabe, C.C. Tasan, Metastable high-entropy dual-phase alloys overcome the strength–ductility trade-off, *Nature* 534 (7606) (2016) 227–230.
- [8] Z. Wu, H. Bei, G.M. Pharr, E.P. George, Temperature dependence of the mechanical properties of equiatomic solid solution alloys with face-centered cubic crystal structures, *Acta Mater.* 81 (2014) 428–441.
- [9] Y. Zhang, Y.N. Osetsky, W.J. Weber, Tunable chemical disorder in concentrated alloys: defect physics and radiation performance, *Chem. Rev.* 122 (2022) 789–829.
- [10] Y. Zhang, T. Egami, W.J. Weber, Dissipation of radiation energy in concentrated alloys: unique defect properties and microstructural evolution, *MRS Bull.* 44 (2019) 798–811.
- [11] Y. Zhang, W.J. Weber, Ion irradiation and modification: the role of coupled electronic and nuclear energy dissipation and subsequent nonequilibrium processes in materials, *Appl. Phys. Rev.* 7 (2020) 041307.
- [12] Z. Fan, S. Zhao, K. Jin, D. Chen, Y.N. Osetskiy, Y. Wang, H. Bei, K.L. More, Y. Zhang, Helium irradiated cavity formation and defect energetics in Ni-based binary single-phase concentrated solid solution alloys, *Acta Mater.* 164 (2019) 283–292.
- [13] C. Lu, L. Niu, N. Chen, K. Jin, T. Yang, P. Xiu, Y. Zhang, F. Gao, H. Bei, S. Shi, M.R. He, I.M. Robertson, W.J. Weber, L. Wang, Enhancing radiation tolerance by controlling defect mobility and migration pathways in multicomponent single-phase alloys, *Nat. Commun.* 7 (1) (2016) 13564.
- [14] C. Lu, T. Yang, K. Jin, N. Gao, P. Xiu, Y. Zhang, F. Gao, H. Bei, W.J. Weber, K. Sun, Y. Dong, L. Wang, Radiation-induced segregation on defect clusters in single-phase concentrated solid-solution alloys, *Acta Mater.* 127 (2017) 98–107.
- [15] Y. Zhang, G.M. Stocks, K. Jin, C. Lu, H. Bei, B.C. Sales, L. Wang, L.K. Béland, R.E. Stoller, G.D. Samolyuk, M. Caro, A. Caro, W.J. Weber, Influence of chemical disorder on energy dissipation and defect evolution in concentrated solid solution alloys, *Nat. Commun.* 6 (1) (2015) 8736.
- [16] Y.N. Osetsky, A.V. Barashev, L.K. Béland, Z. Yao, K. Ferasat, Y. Zhang, Tunable chemical complexity to control atomic diffusion in alloys, *npj Comput. Mater.* 6 (2020) 38.
- [17] M.R. He, S. Wang, K. Jin, H. Bei, K. Yasuda, S. Matsumura, K. Higashida, I.M. Robertson, Enhanced damage resistance and novel defect structure of CrFeCoNi under *in situ* electron irradiation, *Scr. Mater.* 125 (2016) 5–9.
- [18] Y. Zhang, S. Zhao, W.J. Weber, K. Nordlund, F. Granberg, F. Djurabekova, Atomic-level heterogeneity and defect dynamics in concentrated solid-solution alloys, *Curr. Opin. Solid State Mater. Sci.* 21 (5) (2017) 221–237.
- [19] S. Shi, H. Bei, I.M. Robertson, Impact of alloy composition on one-dimensional glide of small dislocation loops in concentrated solid solution alloys, *Mater. Sci. Eng. A* 700 (2017) 617–621.
- [20] T. Yang, Z. Tang, X. Xie, R. Carroll, G. Wang, Y. Wang, K.A. Dahmen, P.K. Liaw, Y. Zhang, Deformation mechanisms of Al<sub>0.1</sub>CoCrFeNi at elevated temperatures, *Mater. Sci. Eng. A* 684 (2017) 552–558.
- [21] T. Yang, S. Xia, W. Guo, R. Hu, J.D. Poplawsky, G. Sha, Y. Fang, Z. Yan, C. Wang, C. Li, Y. Zhang, S.J. Zinkle, Y. Wang, Effects of temperature on the irradiation responses of Al<sub>0.1</sub>CoCrFeNi high entropy alloy, *Scr. Mater.* 144 (2018) 31–35.
- [22] R.W. Harrison, G. Greaves, H. Le, H. Bei, Y. Zhang, S.E. Donnelly, Chemical effects on He bubble superlattice formation in high entropy alloys, *Curr. Opin. Solid State Mater. Sci.* 23 (4) (2019) 100762.
- [23] N. Sellami, A. Debelle, M.W. Ullah, H.M. Christen, J.K. Keum, H. Bei, H. Xue, W.J. Weber, Y. Zhang, Effect of electronic energy dissipation on strain relaxation in irradiated concentrated solid solution alloys, *Curr. Opin. Solid State Mater. Sci.* 23 (2) (2019) 107–115.
- [24] M.R. He, S. Wang, S. Shi, K. Jin, H. Bei, K. Yasuda, S. Matsumura, K. Higashida, I.M. Robertson, Mechanisms of radiation-induced segregation in CrFeCoNi-based single-phase concentrated solid solution alloys, *Acta Mater.* 126 (2017) 182–193.
- [25] C. Lu, T. Yang, K. Jin, G. Velisa, P. Xiu, M. Song, Q. Peng, F. Gao, Y. Zhang, H. Bei, W.J. Weber, L. Wang, Enhanced void swelling in NiCoFeCrPd high-entropy alloy by indentation-induced dislocations, *Mater. Res. Lett.* 6 (10) (2018) 584–591.
- [26] T. Yang, W. Guo, J.D. Poplawsky, D. Li, L. Wang, Y. Li, W. Hu, M.L. Crespillo, Z. Yan, Y. Zhang, Y. Wang, S.J. Zinkle, Structural damage and phase stability of

- Al<sub>0.3</sub>CoCrFeNi high entropy alloy under high temperature ion irradiation, *Acta Mater.* 188 (2020) 1–15.
- [27] K. Jin, H. Bei, Y. Zhang, Ion irradiation induced defect evolution in Ni and Ni-based FCC equiatomic binary alloys, *J. Nucl. Mater.* 471 (2016) 193–199.
- [28] K. Jin, W. Guo, C. Lu, M.W. Ullah, Y. Zhang, W.J. Weber, L. Wang, J.D. Poplawsky, H. Bei, Effects of Fe concentration on the ion-irradiation induced defect evolution and hardening in Ni-Fe solid solution alloys, *Acta Mater.* 121 (2016) 365–373.
- [29] G. Veliša, M.W. Ullah, H. Xue, K. Jin, M.L. Crespiello, H. Bei, W.J. Weber, Y. Zhang, Irradiation-induced damage evolution in concentrated Ni-based alloys, *Acta Mater.* 135 (2017) 54–60.
- [30] G. Veliša, E. Wendler, S. Zhao, K. Jin, H. Bei, W.J. Weber, Y. Zhang, Delayed damage accumulation by athermal suppression of defect production in concentrated solid solution alloys, *Mater. Res. Lett.* 6 (2) (2018) 136–141.
- [31] Z. Fan, G. Velisa, K. Jin, M.L. Crespiello, H. Bei, W.J. Weber, Y. Zhang, Temperature-dependent defect accumulation and evolution in Ni-irradiated NiFe concentrated solid-solution alloy, *J. Nucl. Mater.* 519 (2019) 1–9.
- [32] G. Veliša, K. Jin, Z. Fan, C. Lu, H. Bei, W.J. Weber, L. Wang, Y. Zhang, Multi-axial and multi-energy channeling study of disorder evolution in ion-irradiated nickel, *J. Nucl. Mater.* 525 (2019) 92–101.
- [33] L.M. Howe, M.L. Swanson, A.F. Quenneville, Defect-solute atom interactions in hexagonal close-packed metals as investigated using channeling techniques, *J. Nucl. Mater.* 69 (70) (1978) 744–747.
- [34] M.L. Swanson, L.M. Howe, J.A. Moore, A.F. Quenneville, Defect complexes in ion-irradiated aluminum, *Nucl. Instrum. Methods Phys. Res.* 209 (210) (1983) 1029–1034.
- [35] K. Jin, B.C. Sales, G.M. Stocks, G.D. Samolyuk, M. Daene, W.J. Weber, Y. Zhang, H. Bei, Tailoring the physical properties of Ni-based single-phase equiatomic alloys by modifying the chemical complexity, *Sci. Rep.* 6 (2016) 20159.
- [36] M.L. Crespiello, J.T. Graham, Y. Zhang, W.J. Weber, *In-situ* luminescence monitoring of ion-induced damage evolution in SiO<sub>2</sub> and Al<sub>2</sub>O<sub>3</sub>, *J. Lumin.* 172 (2016) 208–218.
- [37] M.L. Crespiello, J.T. Graham, Y. Zhang, W.J. Weber, Temperature measurements during high flux ion beam irradiations, *Rev. Sci. Instrum.* 87 (2) (2016) 024902.
- [38] Y. Zhang, M.L. Crespiello, H. Xue, K. Jin, C.H. Chen, C.L. Fontana, J.T. Graham, W.J. Weber, New ion beam materials laboratory for materials modification and irradiation effects research, *Nucl. Instrum. Methods Phys. Res. Sect. B* 338 (2014) 19–30.
- [39] Y. Zhang, J. Lian, Z. Zhu, W.D. Bennett, L.V. Saraf, J.L. Rausch, C.A. Hendricks, R.C. Ewing, W.J. Weber, Response of strontium titanate to ion and electron irradiation, *J. Nucl. Mater.* 389 (2) (2009) 303–310.
- [40] K. Jin, G. Velisa, H. Xue, T. Yang, H. Bei, W.J. Weber, L. Wang, Y. Zhang, Channeling analysis in studying ion irradiation damage in materials containing various types of defects, *J. Nucl. Mater.* 517 (2019) 9–16.
- [41] M.W. Ullah, H. Xue, G. Velisa, K. Jin, H. Bei, W.J. Weber, Y. Zhang, Effects of chemical alternation on damage accumulation in concentrated solid-solution alloys, *Sci. Rep.* 7 (1) (2017) 4146.
- [42] J.B.J. Ziegler, M. Ziegler, SRIM-2013 (Stopping and Range of Ions in Matter), 2013. <http://www.srim.org/>.
- [43] W.J. Weber, Y. Zhang, Predicting damage production in monoatomic and multi-elemental targets using stopping and range of ions in matter code: challenges and recommendations, *Curr. Opin. Solid State Mater. Sci.* 23 (4) (2019) 100757.
- [44] G. Kresse & J. Furthmuller Vienna *ab-initio* simulation package (VASP): the guide. (Universität Wien, 2002).
- [45] S. San, Y. Tong, H. Bei, B. Kombaiah, Y. Zhang, W.Y. Ching, First-principles calculation of lattice distortions in four single phase high entropy alloys with experimental validation, *Mater. Des.* 209 (2021) 110071.
- [46] W.Y. Ching, P. Rulis, *Electronic Structure Methods For Complex Materials: the Orthogonalized Linear Combination of Atomic Orbitals*, Oxford University Press, 2012.
- [47] H. Yao, L. Ouyang, W.Y. Ching, Ab initio calculation of elastic constants of ceramic crystals, *J. Am. Ceram. Soc.* 90 (10) (2007) 3194–3204.
- [48] R.S. Mulliken, Electronic population analysis on LCAO-MO molecular wave functions. I, *J. Chem. Phys.* 23 (10) (1955) 1833–1840.
- [49] F.X. Zhang, S. Zhao, K. Jin, H. Xue, G. Velisa, H. Bei, R. Huang, J.Y.P. Ko, D.C. Pagan, J.C. Neufeuind, et al., Local structure and short-range order in a NiCoCr solid solution alloy, *Phys. Rev. Lett.* 118 (2017) 205501.
- [50] Y. Tong, G. Velisa, S. Zhao, W. Guo, T. Yang, K. Jin, C. Lu, H. Bei, J.Y.P. Ko, D.C. Pagan, Y. Zhang, L. Wang, F.X. Zhang, Evolution of local lattice distortion under irradiation in medium- and high-entropy alloys, *Materials* 2 (2018) 73–81.
- [51] Y. Tong, S. Zhao, K. Jin, H. Bei, J.Y.P. Ko, Y. Zhang, F.X. Zhang, A comparison study of local lattice distortion in Ni<sub>80</sub>Pd<sub>20</sub> binary alloy and FeCoNiCrPt high-entropy alloy, *Scr. Mater.* 156 (2018) 14–18.
- [52] Y. Tong, K. Jin, H. Bei, J.Y.P. Ko, D.C. Pagan, Y. Zhang, F.X. Zhang, Local lattice distortion in NiCoCr, FeCoNiCr and FeCoNiCrMn concentrated alloys investigated by synchrotron X-ray diffraction, *Mater. Des.* 155 (2018) 1–7.
- [53] F.X. Zhang, Y. Tong, K. Jin, H. Bei, W.J. Weber, A. Hug, T. Lanzirrott, M. Newville, D.C. Pagan, J.Y.P. Ko, et al., Chemical complexity induced local structural distortion in NiCoFeMnCr high-entropy alloy, *Mater. Res. Lett.* 6 (2018) 450–455.
- [54] Y. Tong, S. Zhao, H. Bei, T. Egami, Y. Zhang, F.X. Zhang, Severe local lattice distortion in Zr- and/or Hf-containing refractory multi-principal element alloys, *Acta Mater.* 183 (2020) 172–181.
- [55] L.C. Feldman, J.W. Mayer, S.T. Picraux, Chapter 4 - dechanneling by defects, in: L.C. Feldman, J.W. Mayer, S.T. Picraux (Eds.), *Materials Analysis by Ion Channeling*, Academic Press, San Diego, 1982, pp. 88–116.
- [56] P. Xiu, H. Bei, Y. Zhang, L. Wang, K.G. Field, STEM Characterization of dislocation loops in irradiated FCC alloys, *J. Nucl. Mater.* 544 (2021) 152658.
- [57] E. Friedland, M. Fletcher, Structure dependence of radiation damage depths after ion implantation, *Nucl. Instrum. Methods Phys. Res. Sect. B Beam Interact. Mater. At.* 64 (1) (1992) 242–245.
- [58] C. Lu, K. Jin, L.K. Béland, F. Zhang, T. Yang, L. Qiao, Y. Zhang, H. Bei, H.M. Christen, R.E. Stoller, L. Wang, Direct observation of defect range and evolution in ion-irradiated single crystalline Ni and Ni binary alloys, *Sci. Rep.* 6 (2016) 19994.
- [59] Y.P. Sharkeev, E.V. Kozlov, The long-range effect in ion implanted metallic materials: dislocation structures, properties, stresses, mechanisms, *Surf. Coat. Technol.* 158 (159) (2002) 219–224.
- [60] M.W. Ullah, Y. Zhang, N. Sellami, A. Debelle, H. Bei, W.J. Weber, Evolution of irradiation-induced strain in an equiatomic NiFe alloy, *Scr. Mater.* 140 (2017) 35–39.
- [61] H. Kudo, Energy dependence of dechanneling by a dislocation loop, *Phys. Rev. B* 18 (11) (1978) 5995–5999.
- [62] Y. Quéré, About the dechanneling due to dislocation loops, *Radiat. Eff.* 38 (3–4) (1978) 131–132.
- [63] S. Moll, L. Thomé, G. Sattonnay, A. Debelle, F. Garrido, L. Vincent, J. Jagielski, Multistep damage evolution process in cubic zirconia irradiated with MeV ions, *J. Appl. Phys.* 106 (7) (2009) 073509.
- [64] B. Yao, D.J. Edwards, R.J. Kurtz, TEM characterization of dislocation loops in irradiated bcc Fe-based steels, *J. Nucl. Mater.* 434 (1–3) (2013) 402–410.
- [65] C.M. Parish, K.G. Field, A.G. Certain, J. Wharry, Application of STEM characterization for investigating radiation effects in BCC Fe-based alloys, *J. Mater. Res.* 30 (2015) 1275–1289.
- [66] P. Xiu, Y.N. Osetsky, L. Jiang, G. Velisa, Y. Tong, H. Bei, W.J. Weber, Y. Zhang, L. Wang, Dislocation loop evolution and radiation hardening in nickel-based concentrated solid solution alloys, *J. Nucl. Mater.* 538 (2020) 152247.
- [67] D.S. Aidhy, C. Lu, K. Jin, H. Bei, Y. Zhang, L. Wang, W.J. Weber, Point defect evolution in Ni, NiFe and NiCr alloys from atomistic simulations and irradiation experiments, *Acta Mater.* 99 (2015) 69–76.
- [68] S.L. Dudarev, K. Arakawa, X. Yi, Z. Yao, M.L. Jenkins, M.R. Gilbert, P.M. Derlet, Spatial ordering of nano-dislocation loops in ion-irradiated materials, *J. Nucl. Mater.* 455 (1–3) (2014) 16–20.
- [69] S. Zhang, K. Nordlund, F. Djurabekova, F. Granberg, Y. Zhang, T.S. Wang, Radiation damage buildup by athermal defect reactions in nickel and concentrated nickel alloys, *Mater. Res. Lett.* 5 (2017) 433–439.
- [70] F. Tuomisto, I. Makkonen, J. Heikinheimo, F. Granberg, F. Djurabekova, K. Nordlund, G. Velisa, H. Bei, H. Xue, W.J. Weber, Y. Zhang, Segregation of Ni at early stages of radiation damage in NiCoFeCr solid solution alloys, *Acta Mater.* 196 (2020) 44–51.
- [71] F. Tuomisto, I. Makkonen, Defect identification in semiconductors with positron annihilation: experiment and theory, *Rev. Mod. Phys.* 85 (2013) 1583–1631.
- [72] S. Zhao, T. Egami, M. Stocks, Y. Zhang, Effect of d electrons on defect properties in equiatomic NiCoCr and NiCoFeCr concentrated solid solution alloys, *Phys. Rev. Mater.* 2 (2018) 013602.
- [73] S. Zhao, G.M. Stocks, Y. Zhang, Defect energetics of concentrated solid-solution alloys from ab initio calculations: Ni<sub>0.5</sub>Co<sub>0.5</sub>, Ni<sub>0.5</sub>Fe<sub>0.5</sub>, Ni<sub>0.8</sub>Fe<sub>0.2</sub> and Ni<sub>0.8</sub>Cr<sub>0.2</sub>, *Phys. Chem. Chem. Phys.* 18 (2016) 24043–24056.
- [74] Y.N. Osetskiy, L. Beland, A. Barashev, Y. Zhang, On the existence and origin of sluggish diffusion in chemically disordered concentrated alloys, *Curr. Opin. Solid State Mater. Sci.* 22 (2018) 65–74.
- [75] E. Lu, J. Zhao, I. Makkonen, K. Mizohata, Z. Li, M. Hua, F. Djurabekova, F. Tuomisto, Enhancement of vacancy diffusion by C and N interstitials in the equiatomic FeMnNiCoCr high entropy alloy, *Acta Mater.* 215 (2021) 117093.
- [76] S. Zhao, G.M. Stocks, Y. Zhang, Stacking fault energies of face-centered cubic concentrated solid solution alloys, *Acta Mater.* 134 (2017) 334–345.
- [77] A.D. Brailsford, L.K. Mansur, Effect of self-ion injection in simulation studies of void swelling, *J. Nucl. Mater.* 71 (1977) 110–116.
- [78] M.P. Short, D.R. Gaston, M. Jin, L. Shao, F.A. Garner, Modeling injected interstitial effects on void swelling in self-ion irradiation experiments, *J. Nucl. Mater.* 471 (2016) 200–207.
- [79] L. Shao, C.C. Wei, J. Gigax, A. Aitkaliyeva, D. Chen, B.H. Sencer, F.A. Garner, Effect of defect imbalance on void swelling distributions produced in pure iron irradiated with 3.5 MeV self-ions, *J. Nucl. Mater.* 453 (2014) 176–181.
- [80] O. Tissot, C. Pareige, E. Meslin, B. Décamps, J. Henry, Influence of injected interstitials on  $\alpha'$  precipitation in Fe–Cr alloys under self-ion irradiation, *Mater. Res. Lett.* 5 (2) (2017) 117–123.
- [81] T.N. Yang, C. Lu, K. Jin, M. Crespiello, Y. Zhang, H. Bei, L. Wang, The effect of injected interstitials on void formation in self-ion irradiated nickel containing concentrated solid solution alloys, *J. Nucl. Mater.* 488 (2017) 328–337.
- [82] S. Moll, L. Thomé, L. Vincent, F. Garrido, G. Sattonnay, T. Thomé, J. Jagielski, J.M. Costantini, Damage induced by electronic excitation in ion-irradiated yttria-stabilized zirconia, *J. Appl. Phys.* 105 (2) (2009) 023512.
- [83] S. Moll, Y. Zhang, A. Debelle, L. Thomé, J.P. Crocombette, Z. Zihua, J. Jagielski, W.J. Weber, Damage processes in MgO irradiated with medium-energy heavy ions, *Acta Mater.* 88 (2015) 314–322.
- [84] J. Jagielski, L. Thomé, Multi-step damage accumulation in irradiated crystals, *Appl. Phys. A* 97 (1) (2009) 147–155.
- [85] C. Mieszczyński, R. Ratajczak, J. Jagielski, G. Veliša, H. Bei, B.C. Sales, E. Wendler, W.J. Weber, Y. Zhang, Defect evolution in Ni and solid-solution alloys of NiFe and NiFeCoCr under ion irradiation at 16 and 300K, *J. Nucl. Mater.* 534 (2020) 152138.
- [86] X. Jin, A. Boule, A. Chartier, J.P. Crocombette, A. Debelle, Analysis of strain and disordering kinetics based on combined RBS-channeling and X-ray diffraction

- atomic-scale modelling, *Acta Mater.* 201 (2020) 63–71.
- [87] W.J. Weber, N. Yu, L.M. Wang, Irradiation-induced amorphization in  $\beta$ -SiC, *J. Nucl. Mater.* 253 (1) (1998) 53–59.
- [88] J. Olivares, G. García, F. Agulló-López, F. Agulló-Rueda, A. Kling, J.C. Soares, Generation of amorphous surface layers in  $\text{LiNbO}_3$  by ion-beam irradiation: thresholding and boundary propagation, *Appl. Phys. A* 81 (7) (2005) 1465–1469.
- [89] A. Rivera, M.L. Crespillo, J. Olivares, G. García, F. Agulló-López, Effect of defect accumulation on ion-beam damage morphology by electronic excitation in lithium niobate: a Monte Carlo approach, *Nucl. Instrum. Methods Phys. Res. B* 268 (13) (2010) 2249–2256.

Edit

Proof

PDF